nature communications

Article

https://doi.org/10.1038/s41467-024-51014-4

Motion blur microscopy: in vitro imaging of cell adhesion dynamics in whole blood flow

Received: 11 November 2023

Accepted: 26 July 2024

Published online: 16 August 2024

Check for updates

Utku Goreke[1], Ayesha Gonzales[2,4], Brandon Shipley[2,4], Madeleine Tincher[3], Oshin Sharma[1], William J. Wulftange[3], Yuncheng Man[1], Ran An[1], Michael Hinczewski[2] ✉ & Umut A. Gurkan[1,3] ✉

Imaging and characterizing the dynamics of cellular adhesion in blood samples is of fundamental importance in understanding biological function. In vitro microscopy methods are widely used for this task but typically require diluting the blood with a buffer to allow for transmission of light. However, whole blood provides crucial signaling cues that influence adhesion dynamics, which means that conventional approaches lack the full physiological complexity of living microvasculature. We can reliably image cell interactions in microfluidic channels during whole blood flow by motion blur microscopy (MBM) in vitro and automate image analysis using machine learning. MBM provides a low cost, easy to implement alternative to intravital microscopy, for rapid data generation where understanding cell interactions, adhesion, and motility is crucial. MBM is generalizable to studies of various diseases, including cancer, blood disorders, thrombosis, inflammatory and autoimmune diseases, as well as providing rich datasets for theoretical modeling of adhesion dynamics.

Cellular interactions, including cell adhesion, migration, and chemotaxis, are important in investigating the mechanisms of diseases including cancer, thrombosis, inflammatory diseases, anemia, and vasculopathy. In vitro cellular imaging techniques for hematology generally require the use of an aqueous buffer[1–3], which dilutes the sample and allows transmission of light for imaging[4]. However, buffer solutions replace the original whole blood medium, potentially affecting the biological mechanisms under investigation. For instance, plasma proteins facilitate the interaction of red blood cells with endothelial cells, and red blood cells induce margination of leukocytes and platelets to the vascular wall[5,6]. Comprehensively understanding these phenomena requires a physiologically realistic approach that includes the presence of whole blood. Therefore, intravital methods remain the gold standard for studies of important dynamic processes associated with cellular interactions[7]. Intravital methods include multi- and single-photon microscopy, confocal microscopy, Brillouin spectroscopy combined with light microscopy, lightsheet microscopy, and endomicroscopy[8–13]. However, intravital microscopy methods are highly costly, and require intensive effort in both setup and analysis, and therefore have limited applicability for the broader research community[14,15]. Total internal reflection fluorescence microscopy is a potential in vitro alternative for visualizing cellular interactions under whole blood flow (and examples with buffer flow already exist[16,17]). But fluorophore labeling in whole blood can be challenging. Finally, laser optical imaging has been used for obtaining the number of platelet interactions that occur with a protein substrate in a microfluidic channel[18], but this method is limited to a single numeric output (intensity of light scattered over time) and has additional experimental setup complexity.

Here, we describe a practical, accessible, and easily adaptable microscopy method that enables real-time imaging of dynamics of cellular interactions under whole blood flow in vitro by completely eliminating the need for blood sample dilution. We call our approach motion blur microscopy (MBM). MBM leverages blurring to make the cellular interactions that take place at slower velocity scales discernable (Fig. 1). For simplicity, we showcase MBM on protein functionalized surfaces, but MBM also works on endothelialized surfaces. We show that the numbers of adhesive sickle red blood cells (sRBCs) from

[1]Department of Mechanical and Aerospace Engineering, Case Western Reserve University, Cleveland, OH, USA. [2]Department of Physics, Case Western Reserve University, Cleveland, OH, USA. [3]Department of Biomedical Engineering, Case Western Reserve University, Cleveland, OH, USA. [4]These authors contributed equally: Ayesha Gonzales, Brandon Shipley. ✉e-mail: michael.hinczewski@case.edu; umut.gurkan@case.edu

individuals with sickle cell disease interacting with the endothelial surface are greater than those of healthy RBCs, and diluting the whole blood samples may diminish these interactions or result in aberrant interactions (Fig. 2). Individual cells with a velocity substantially less than the bulk flow (i.e., immobile, adhered cells, or those that are rolling/migrating while in contact with the surface) can be visualized within the whole blood flow. MBM allows in vitro analysis of various static and dynamic properties of cellular interactions, all while mimicking key in vivo conditions.

MBM works by reducing the light source and increasing the exposure time, resulting in streaks of flowing cells that generate noisy images. Thus, to identify and analyze adhered cells, an experimenter must spend a considerable amount of time and effort to distinguish cells. While this may not be a difficult task when analyzing individual MBM images, manually analyzing dynamic interactions from MBM videos consisting of hundreds or thousands of frames can be impractical and error-prone. Therefore, we developed an automated machine-learning-based analysis, which can efficiently characterize the dynamics of cellular interactions in MBM videos. The automated analysis is a two-phase system, where phase one identifies groups of pixels in an MBM image corresponding to adhered cells, and phase two classifies these groups by cell type (Fig. 3a). The phase one task is completed using a machine learning segmentation network. The phase two task is completed by classifying cells by their size, or by using a machine learning classification network, depending on the complexity of the system under study. Figure 3b–e shows examples of adhered regions that one might expect the automated analysis to classify. Figure 3b, c corresponds to regions of interest, containing sRBCs and chimeric antigen receptor T-cell (CAR-T) cells, respectively, and the automated analysis should correctly identify these regions as adhered cells. Figure 3d depicts a typical object adhered to the surface that is not protein functionalized, and Fig. 3e shows other stationary objects

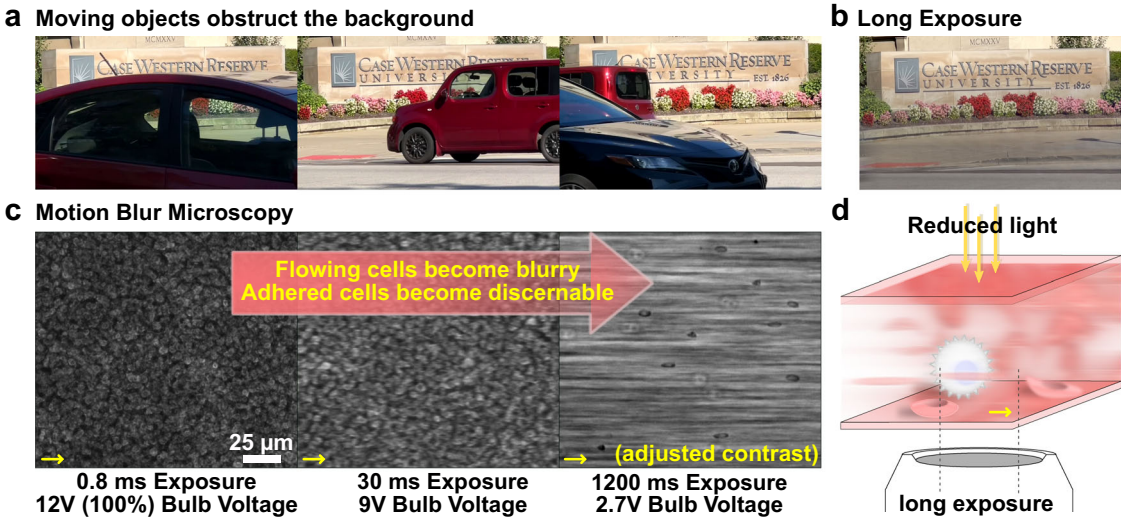

Fig. 1 | Motion blur microscopy (MBM). a Moving objects in the foreground obstruct the stationary objects in the background. **b** By adjusting the exposure, moving objects are blurred to obtain a clear view of the background. **c** The same principle is applied to microscale whole blood flow. Shown are three views of whole blood flow in the same microscopic field with different microscope settings. Increasing the camera exposure (integration time) helps blur the foreground, which consists of non-adhered (flowing) cells. Long exposure results in excess brightness which is then compensated by a reduction of the light source voltage to obtain a clear view of the adhered cells in the background. Yellow arrows show the flow direction. The shear rate of the flow is 50 s^{-1} which is enough to induce the blur at 1200 ms integration time. **d** Schematic illustration of the microfluidic channel, with clearly visible adhered cells and blurry flowing cells.

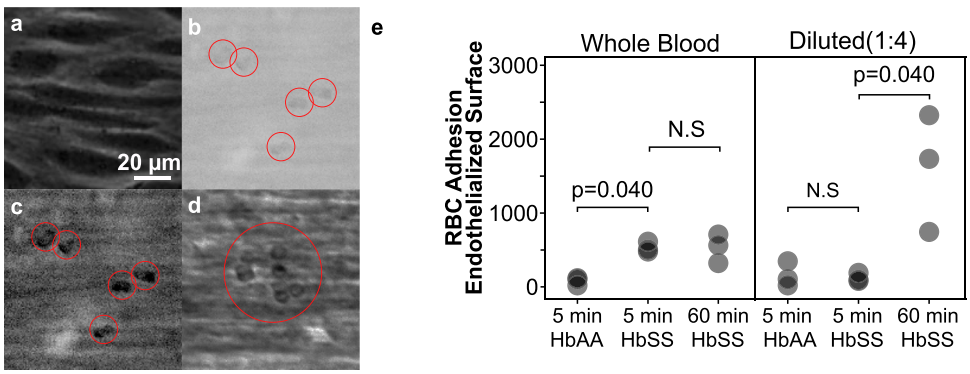

Fig. 2 | MBM allows capturing cellular interactions on endothelial layers and PBS dilution diminishes the sickle RBC adhesion events. a Human umbilical vein endothelial cell (HUVEC) layer on the microfluidic device surface without blood flow. **b** Original MBM images of sickle red blood cells (RBCs) on the endothelial surface, shown without gray histogram adjustment. **c** MBM image shown in inset (**b**) after stretching the histogram to its limits. **d** Aberrant cellular aggregations in diluted flow. **e** Under whole blood flow the number of adhered HbSS RBCs was significantly greater than HbAA RBCs. The number of adhered RBCs did not increase after extended flow duration. On the other hand, the dilution of the HbSS whole blood resulted in similar adhesion in HbAA and HbSS samples. Moreover, extended flow duration significantly increased the RBC adhesion through aberrant cellular interactions such as clumping. Red circles denote locations of adhered RBCs. The scale bar applies to all images. $n = 3$, biological replicates, p-values are calculated with one-tailed Mann–Whitney with ties and continuity correction.

https://doi.org/10.1038/s41467-024-51014-4

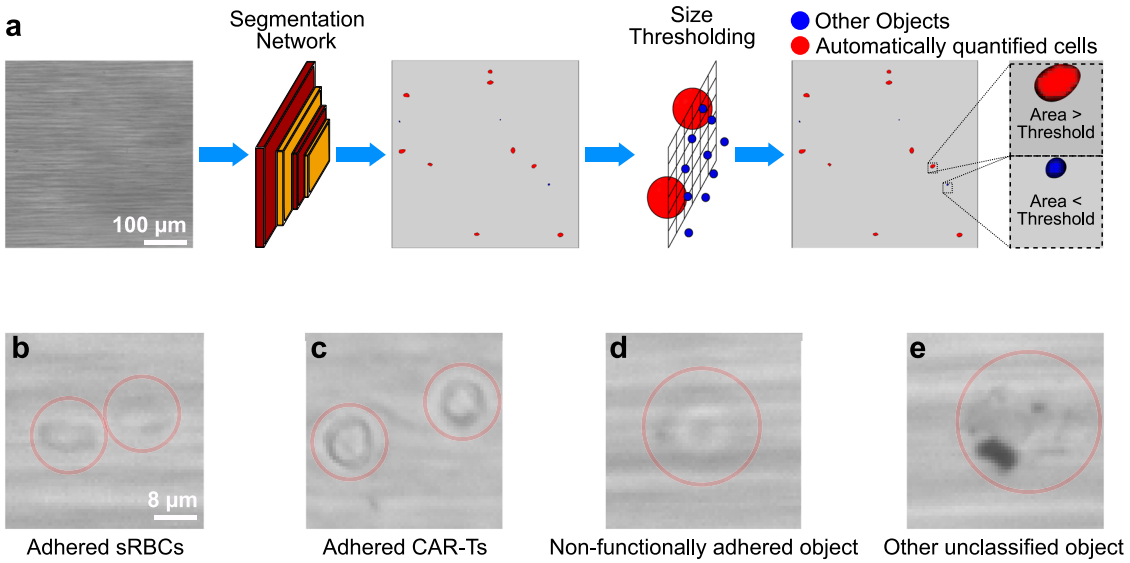

Fig. 3 | Cartoon diagram of automated analysis pipeline and example objects. **a** The pipeline is conducted in two distinct phases. In the first phase (segmentation network), groups of adhered pixels that may correspond to an adhered cell are identified. In the second phase (size thresholding), these groups are classified by cell type. **b**–**e** Four examples of adhered objects that might appear in MBM images. (**b**, **c**) show cells of interest, while (**d**, **e**) show non-relevant adhered regions.

that are not cells. The automated analysis pipeline distinguishes these non-functionally adhered objects and other non-cell objects from the adhered cells of interest.

With our automated analysis, we can process MBM images in an accurate and high throughput manner. Adhered cells can be identified, and morphological features, such as the size and eccentricity of each individual cell can be extracted. MBM videos enable studying the dynamics of cells on the individual level and allow us to determine kinetic properties like adhesion durations and average velocities (for the case of cells that roll or migrate while on the surface). The individual cell data can be aggregated to produce group statistics, such as distributions of morphological features and dynamic quantities, or mean squared displacements. Importantly, the method allows us to identify and analyze the properties of hundreds of thousands of cells. These data can be used to help us understand cellular adhesion dynamics, or be used in clinical studies. Since our approach relies on a basic experimental microscopy setup, we anticipate that it will be highly accessible to the broader research community.

Results and discussion

Characterizing fundamental cellular interactions on the single-cell level can reveal small sub-populations of cells that initiate pathogenesis. Here, we focus on two diseases where the cellular interactions in the vascular space carry central importance. Analyzing these sub-populations typically requires intravital microscopy, and thus, serves as a means to demonstrate the effectiveness of MBM in challenging applications. The first of these diseases is sickle cell disease, where hemoglobin, the fundamental protein underlying red blood cells' oxygen transport, polymerizes in a deoxygenated environment. When the hemoglobin polymerizes, a cascade of events can occur, leading to a debilitating disease complication known as a vaso-occlusive crisis. Red blood cells containing polymerized sickle hemoglobin experience physical and chemical changes, resulting in abnormally stiff, dense, and adhesive cells[19–21]. The second disease in focus is malignant solid tumors where T-cell migration is crucial for immunotherapy of this type of malignancy. Many CAR-T therapies are under development for solid tumors, and they hold great promise for treating refractory cancers. Understanding the migration of T cells, specifically CAR-T cells, would lead to better design of future cell therapies when diapedesis/migration is an important aspect of the therapy, as in the case of solid tumors. An accessible, reliable, single-cell level in vitro method for analyzing CAR-T cell behavior, like MBM, would accelerate overcoming this bottleneck.

To demonstrate MBM and put its validity to the test, three distinct experimental setups were used. One experimental setup used a laminin-functionalized channel to observe sRBCs under flow. A second experimental set-up used an E-selectin functionalized channel to observe CAR-T cells under flow. The final experimental set-up used a P-selectin functionalized channel to observe a combination of red blood cells and CAR-T cells under flow. We include this final set-up as an additional demonstration of the flexibility of MBM, and the details of its analysis are in the Supplementary Information (SI). In this work, we aim to accomplish three main goals. One, we show that MBM with automated analysis is accurate, insofar as it can correctly classify cells for a variety of inputs in a reproducible manner. Two, we show that relevant physical properties of identified cells can be determined. Three, we show that the identified cells and their properties constitute a data set with practical uses, ranging from studying cellular adhesion mechanics to aiding in clinical studies.

Overview of MBM with automated analysis

Here we summarize the complete process for analyzing blood samples using MBM (full details can be found in the Methods and SI). Given a cell type (or types) of interest, we functionalize a microchannel with suitable adhesion proteins. Blood samples sent through the microchannels are then imaged to produce either individual MBM images or videos. Cells of interest adhere to the functionalized protein surfaces and become visible against the blurred foreground of non-adhered flowing cells. The MBM images are analyzed via a two-stage automated process schematically illustrated in Fig. 3a. The first phase consists of a segmentation neural network, which labels pixels from MBM images corresponding to adhered objects, and groups together neighboring labeled pixels. In phase two of the analysis, groups of labeled pixels are then classified by cell type using either a size threshold (in applications where size is a sufficient criterion) or a specially trained classification neural network (in more complicated scenarios). After all of the cells in an MBM image or MBM video have been identified, we then generate data for each identified cell. Morphological properties like the size and eccentricity of each cell can be extracted, as well as dynamical properties such as adhesion duration or mean velocity. Using the

https://doi.org/10.1038/s41467-024-51014-4

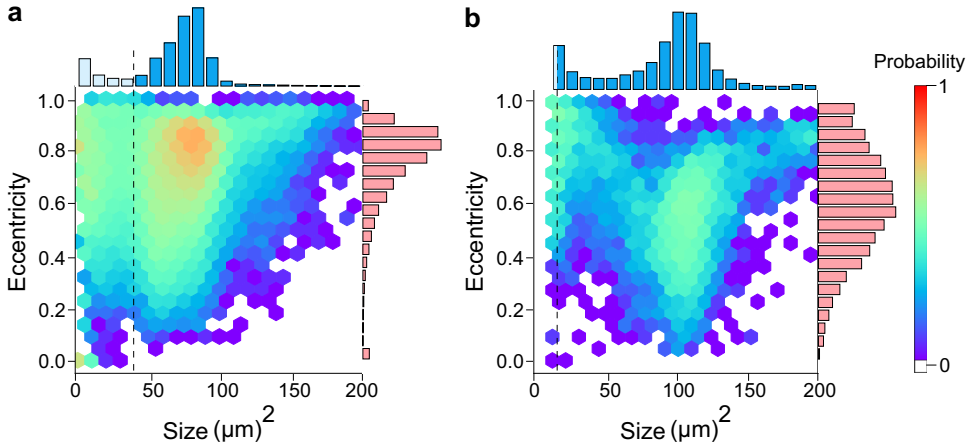

Fig. 4 | Size and eccentricity distributions under whole blood flow. Joint probability distributions for the size and eccentricity of (**a**) objects adhered to laminin functionalized channels from 174 images ($N = 162{,}207$) and (**b**) objects adhered to E-selectin functionalized channels from 2 videos ($N = 5919$). Marginal distributions of size and eccentricity are shown on the top and right axes respectively. Dotted vertical lines indicate the size threshold used for classification, with objects above the threshold corresponding to sRBCs in panel (**a**) or CAR-T cells in panel (**b**).

automated analysis, we were able to extract properties of individual cells for sRBC/laminin images and videos, a CAR-T/P-selectin video, and CAR-T/E-selectin videos, all together containing hundreds of thousands of adhesion events.

MBM-based cell classification is reproducible and accurate

In cases where only a single cell type is expected to be visible in an MBM image, we demonstrate that we can distinguish groups of adhered pixels identified by the phase one segmentation network from debris and other artifacts using morphological properties of the group.

In Fig. 4, we show joint probability densities of the size and eccentricity of all groups of adhered pixels identified by the segmentation network for two collections of MBM images: sRBC adhesion to laminin (Fig. 4a) and CAR-T adhesion to E-selectin (Fig. 4b). The histograms on the top and right edges of the figures are marginal distributions of either the size or eccentricity alone. The joint probabilities reveal three distinct classes of objects: small size/high eccentricity, small size/zero eccentricity, and large size/high eccentricity. The last category corresponds to sRBC or CAR-T cells, and hence we can use a size threshold (indicated by dashed vertical lines) to distinguish cells from other adhered objects (i.e., debris). Each group of pixels above the threshold is classified as a cell.

To validate the inter-experimenter reproducibility of this classification scheme, two researchers replicated five consecutive experiments each. The experimenters used a single tube of blood collected from a homozygous sickle-cell disease subject and analyzed the number of sRBCs using the MBM approach five times, each over a fifteen minute period per experiment. The results did not show a significant difference between the experimenters (Fig. 5a, $p = 0.934$, two-way ANOVA with replication). Furthermore, the coefficient of variation within the replications of each experimenter was <25% for all but one data point (Fig. 5b), an important precision benchmark for bioanalytical method validation[22]. Collectively, these results provide reasonable assurance for the acquisition of meaningful results by showing that our experimental procedure and analysis pipeline are precise and independent of the experimenter.

Finally, we tested the accuracy of the procedure in counting cells, by comparing manual human and automated counts of adhered cells in various MBM images for both sRBC adhesion to laminin (Fig. 5c, $N = 174$) and CAR-T adhesion to E-selectin (Fig. 5d, $N = 169$). The pipeline performed very well, with an R^2 value of 0.99 for both the sRBC and CAR-T cases. Importantly, the counts remained accurate even as the number of adhered cells becomes large in an individual image.

MBM can provide high-throughput single-cell dynamic data

The effectiveness of MBM at analyzing adhered cells in static images generalizes to videos, allowing us to characterize the dynamics of adhered cells on protein-functionalized surfaces. To facilitate this, we combined the classification procedure described above (applied to each frame of the video) with a cell tracking algorithm, described in detail in the SI. The tracking analysis distinguishes the motion of adhered cells between sequential frames from new adhesion events and quantifies the total time spent by a cell on the surface before detachment.

We show eight representative cell trajectories in Fig. 6a, b, four for sRBC adhesion to laminin, and four for CAR-T cell adhesion to E-selectin. We highlight three distinct types of adhesion events: adhesion events with large displacements, adhesion events with small displacements in the same direction as the flow, and adhesion events with small displacements in the opposite direction of the flow. These trajectories are generated for each adhered cell in an MBM video, giving us a high-throughput approach to collect dynamical information about large numbers of cells.

The adhesion duration distributions in Fig. 7 are one example of the dynamical data that can be compiled through our method, corresponding to thousands of individual trajectories. Figure 7a shows sRBC adhesion to laminin, and Fig. 7b shows CAR-T cell adhesion to E-selectin. In both cases there is a peak in the distribution at low adhesion durations, corresponding to a large number of rapid attachment/detachment events, but also a non-trivial proportion of long-lived trajectories. At intermediate times, both plots are approximately power-law. At long times, the sRBC case continues the power-law trend, while CAR-T cells experience more rapid decay. The power law trend also applied to HbAA RBCs from healthy donors without known hemoglobinopathies for short-lived RBC adhesion events and was independent of oxygenation conditions for both HbSS and HbAA RBCs (Supplementary Fig. 5). The longest adhesion durations (hundreds of seconds) occur infrequently, but the number of events collected by MBM is sufficiently large to resolve these rare cases. Adhesion duration distributions are essential raw data for biophysical modeling of bond dynamics between cells and surface proteins under flow conditions, providing a valuable starting point for future studies.

MBM also has the potential of revealing more subtle dynamical relationships that have not been systematically explored, for example how morphological features of cells are correlated with dynamical behaviors at the single-cell level. A longstanding question about sRBCs is whether elongated, irreversibly sickled cells are more adhesive to

https://doi.org/10.1038/s41467-024-51014-4

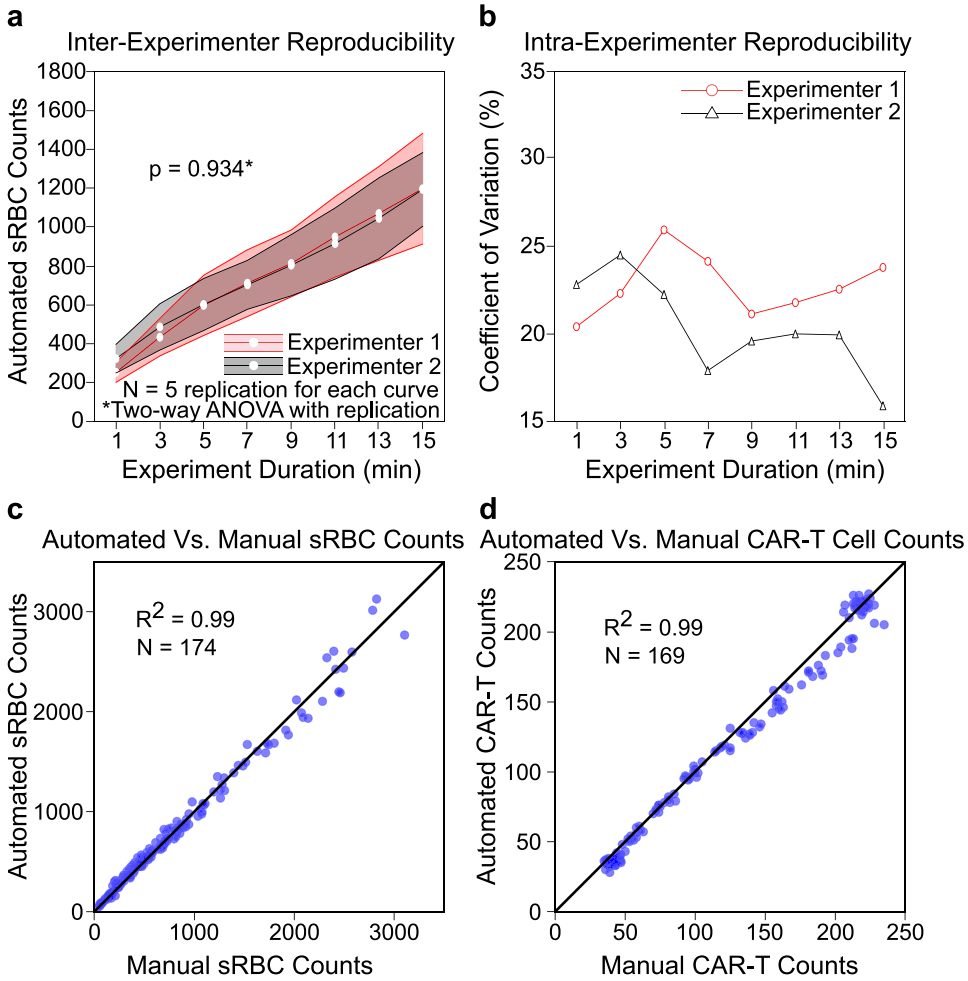

Fig. 5 | Validation and benchmarking of MBM. a We establish inter-experimenter reproducibility for adhered sickle red blood cell (sRBC) counts for different experimental durations, carried out by two different researchers. Shaded regions around each line are one standard deviation, dots represent the average count for each researcher. The cell adhesion results show no significant difference when two different experimenters perform MBM using the aliquots of the same patient sample. **b** We establish the sensitivity of MBM for adhered sRBC counts. For all but one data point, the coefficient of variation is <25%, an important benchmark for the precision of bioanalytical methods. Finally, we establish the accuracy of MBM in counting (**c**) sRBCs adhered to laminin and (**d**) CAR-T cells adhered to E-selectin, respectively. There is a strong agreement between automated and human counts in both cases, as indicated by the R^2 value being close to one.

endothelium than sickle discocytes[23]. In Fig. 8a, we show MBM data for the relationship between average sRBC eccentricity (calculated over the entire cell trajectory) and adhesion duration to laminin, revealing a significant negative trend ($p < 0.03$, linear regression): cells with longer adhesion durations are slightly less elongated on average. In Fig. 8b, we show that such a trend is not statistically significant between average eccentricity and adhesion duration to E-selectin for CAR-T cells ($p > 0.07$, linear regression).

We can also investigate how the orientation of the cell motion relative to the flow direction influences the dynamics. For each cell trajectory, the initial and final position (before detachment) defines a net displacement, which divided by adhesion duration gives us an average velocity vector. The left column of Fig. 9 shows distributions of the components of this vector parallel to and perpendicular to the flow direction. Moreover, we can correlate the average velocity components with adhesion duration (right column of Fig. 9).

This analysis reveals a variety of interesting features. The left panel of Fig. 9a shows sRBC velocities on laminin, projected parallel to the flow direction. The distribution is peaked at zero velocity but has contributions from both positive (with flow) and negative (against flow) velocities. As expected, the distribution is distinctly asymmetric: cells are less likely to move against the flow. The right panel of Fig. 9a bins the sRBCs by adhesion duration and depicts the average parallel velocity for each bin. The shortest adhesion durations have the largest velocities, in agreement with the sample trajectories of Fig. 6a. For velocities perpendicular to the flow direction (Fig. 9b, left) the asymmetry in the distribution vanishes: average velocities in either the up or down perpendicular direction are equally likely. The large tail at positive velocities that was visible in the parallel distribution also disappears. In order to achieve velocities with magnitudes much greater than 2 μm/s one clearly requires the assistance of flow in the same direction as the cell motion.

Figure 9c analyzes the motility of CAR-T cells adhered to E-selectin, parallel to the flow direction. We noted in Fig. 6 that CAR-T cells appeared to be more mobile than sRBCs, and this characteristic is validated in the distribution of average velocities (Fig. 9c, left). Relative to the velocity distribution of sRBCs (Fig. 9a, left), we see about an order of magnitude higher probabilities at short-intermediate positive velocities. In fact, there is a subsidiary peak in the CAR-T distribution around 2 µm/s, in addition to the zero-velocity peak. This trend is also evident when looking at the correlation of velocity with adhesion duration (Fig. 9c, right). On top of the overall trend of shorter adhesion

https://doi.org/10.1038/s41467-024-51014-4

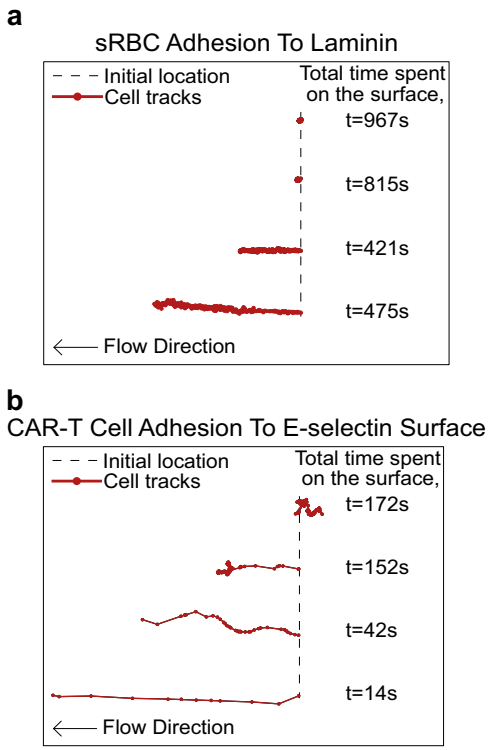

Fig. 6 | Example adhered cell trajectories. Shown are (**a**) sickle red blood cell (sRBC) motion on laminin and (**b**) CAR-T cell motion on E-selectin. Generally speaking, the longer a cell is adhered, the smaller the displacement of the cell in the direction of the flow. CAR-T cells tend to have higher motility relative to sRBCs.

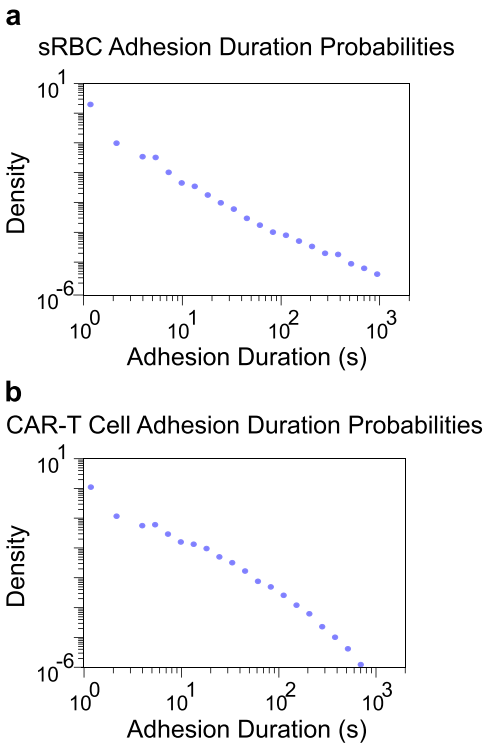

Fig. 7 | Probability distributions of adhesion durations. Shown are (**a**) sickle red blood cell (sRBC) adhesion to laminin ($N = 14{,}229$) and (**b**) CAR-T cell adhesion to E-selectin ($N = 7671$).

durations associated with higher velocities, we see that CAR-T cells experience an order of magnitude higher velocity at short-intermediate adhesion durations relative to sRBCs.

Figure 9 is just one illustration of the versatility of MBM as an in vitro platform for blood cell motility analysis, which to date has been exclusively performed with intravital microscopy. Another promising area for exploration is the impact of environmental signals on motility, for example, CD19 activation of CAR-T cells. The majority of CAR-T cells evaluated for B-cell malignancies target CD19. T cells express programmed cell death protein 1 (PD-1) during activation and You et al. used intravital microscopy to show that T cell motility was proportional to PD-1 expression[24,25]. As an in vitro alternative, we compare CAR-T velocities on E-selectin (parallel to the flow) with and without CD19 activation by using MBM (Fig. 10). Figure 10a shows the velocity distribution for unactivated cells as a control reference, the same distribution as in Fig. 9c but plotted on a linear scale. The velocity bins are color-coded by different velocity regimes. In the absence of CD19 activation, adhered cells fall mainly into relatively immobile populations (the peak around zero velocity, highlighted in purple) and those moving at below 2 μm/s (light blue). As expected, the small velocity population consists mainly of cells that adhere at one location, while the mobile cells show a range of trajectory lengths. CD19 activation significantly enhances the mean velocity of CAR-T cells rolling on E-selectin (Fig. 10b, c, $p < 0.001$, t-test). We also use the same color scale to label and show the trajectories in Fig. 10d, e by their respective velocity regimes. Notably, more complicated motile leukocyte behavior such as crawling can also be captured with MBM (Supplementary Fig. 6 and Supplementary Movie 1).

Microfluidics holds great promise for research into the cellular interactions that take place in blood, and as a result, various microscopy approaches have been developed which complement microfluidic systems. Yet faithfully recreating in vivo conditions in microfluidics is a challenging task, and a bottleneck for its wider adoption. The further a microfluidic study veers from true-to-life conditions, the less physiologically relevant the results become. Therefore, if we are to generate truly meaningful results under in vitro conditions, our methods should strive to reproduce the environment of the microvasculature as much as possible. Researchers have developed a variety of approaches to mimic the microvasculature[26,27], but the blood—the main constituent with its full complexity—has always been missing in these microfluidic systems. MBM enables researchers to investigate the dynamics of cellular interactions in the presence of whole blood flow. This means that many of the relevant physical forces and biochemical signals which modulate cellular interactions will be present during an experiment. Environmental completeness would be especially crucial when the functional pathways of cells are actively regulated by their environment. One example of such regulation is the influence of the complement and renin-angiotensin systems on leukocyte function[28]. Therefore, we anticipate that MBM will have a formative effect on microfluidic studies. Even so, a new method is only as good as the available tools for analysis. Our machine learning pipeline for MBM can automatically analyze hundreds of thousands of observed adhesion events. Typically, the task of completing this analysis manually would be impossible, as the amount of time required, or the number of people required, would be far too large. Our automated analysis approach is flexible and mitigates errors due to individual human biases in cell counting and classification.

The applications of MBM are wide-ranging for both fundamental investigations into biophysical mechanisms and clinical studies. For example, adhesion duration distributions are crucial for studies of force-dependent binding/unbinding of protein complexes and cell-cell interactions[29]. MBM can complement existing approaches in this area like numerical simulations or force spectroscopy experiments (i.e., atomic force microscopy)[30–36]. MBM could provide a valuable comparison point for bond lifetime simulations, adding extra physiological realism due to the blood flow. Because of its ease of implementation, it

https://doi.org/10.1038/s41467-024-51014-4

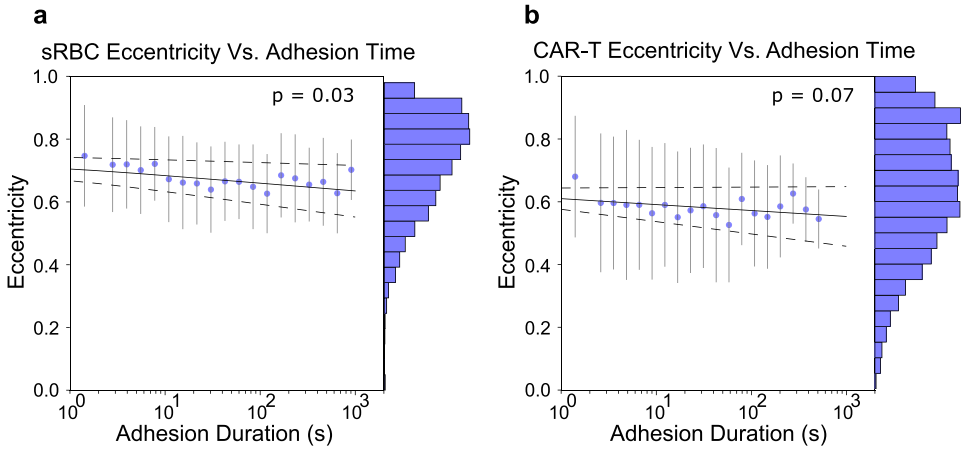

Fig. 8 | Relationships of adhesion duration and morphological features of adhered cells under whole blood flow. Average eccentricity vs. adhesion duration for (**a**) sickle red blood cell (sRBC) adhesion to laminin under normoxic conditions ($N = 14{,}229$), and (**b**) CAR-T cell adhesion to E-Selectin ($N = 5919$). Dotted lines show 95% confidence intervals for the line of best fit. The blue histograms show the distribution of average eccentricities. There is a significant negative relationship between average eccentricity and adhesion duration for sickle RBCs, but not for CAR-T cells ($p = 0.03$, $p = 0.07$, each panel respectively, linear regression). Blue dots represent means, and whiskers for each scatter point are one standard deviation.

is also accessible to a broader research community than atomic force microscopy techniques. On the clinical front, there are a variety of promising applications for specific diseases. In the case of cancer, MBM could help visualize crucial interactions of circulating tumor and endothelial cells with improved physiological accuracy[37]. It can also be utilized to distinguish and isolate rare circulating tumor cells from billions of other cells flowing through a microfluidic channel. For sickle cell disease, MBM could serve as a means to understand how sRBCs behave under changes in blood pressure, flow rates, and viscosity, as well as concentrations of relevant constituents in whole blood. Furthermore, the concentration of adhered sRBCs, as well as the morphological characteristics of the cells may be used to monitor if an individual with sickle cell disease is undergoing a flare-up, or if they are in an asymptomatic diseased state. Other possible disease contexts where MBM may be useful are solid tumor malignancies. MBM may help us characterize the motility of immune cells including T-cells and macrophages with great physiological relevance. As a final example, MBM could be used to further our understanding of autoimmune diseases, such as rheumatoid arthritis, where leukocyte recruitment is an important part of the pathology. For example, MBM can be used in tandem with joint on a chip systems, where complex interactions among blood cells, endothelium, and skeletal components are studied with in vitro experiments[38].

Aside from clinical studies, MBM with automated analysis has the ability to efficiently gather large quantities of data that may provide an ideal basis for theoretical modeling of cellular adhesion mechanics. For example, the velocity distributions parallel to the flow direction from Fig. 9 qualitatively resemble those of molecular motors that are capable of forward and backward stepping along a cytoskeletal track, which can be described via coarse-grained kinetic models of the underlying biochemical cycle[39]. Similar mathematical approaches could be brought to bear on the cell velocity data, giving us a more complete picture of the cell interactions with the endothelium that give rise to these kinds of dynamics. The excellent statistics of the data set is crucial in this regard since in principle it enables us to distinguish between competing models.

As with any experimental approach, there are also limitations. In sufficiently complex scenarios where large densities and/or multiple cell types adhere to the surface, extracting single-cell dynamical information may become more difficult. Large densities, with many overlapping adhered cells, could impede the video analysis in determining if two cells in consecutive frames are the same or not. Overlaps were rare in the examples we investigated, allowing for straightforward extraction of cell trajectories. In physical systems where this would be an issue, however, more sophisticated methods could be incorporated into MBM analysis workflow for tracking cells[40,41]. Similarly, both the sRBC and CAR-T datasets we focused on in the main text involve a single adhered cell type, which could be identified reliably using a size threshold. In cases with multiple cell types of similar sizes, we would have to employ a more involved classification procedure, using other morphological characteristics of the cells. The SI shows results from one such example, where a convolutional neural network was trained to reliably distinguish CAR-T cell adhesion to P-selectin from red blood cells, which also adhere to the surface. Thus we believe all these limitations may be substantially addressed with additions to the data analysis approach. Extended exposure time inherently offsets the eccentricity estimations of the interacting cells. The magnitude of the offset would depend on the velocity of the cells. Eccentricity estimation of high motility cells including T-cells may be significantly affected by this issue. In a typical scenario, a perfectly round CAR-T cell with a size of 8 µm, moving with a mean velocity of 2 µm/s would travel 2.4 µm during the 1200 ms exposure time of the camera. In this case, the resulting eccentricity estimate would be offset by 0.32. This effect can be accounted for using a velocity-based calibration curve for the major axis a, during the eccentricity e calculation:

$$e = \sqrt{1 - b^2/a_{\mathrm{corr}}^2} \tag{1}$$

where b is the minor axis length and the corrected major axis length a_{corr} would be given by:

$$a_{\mathrm{corr}} = a_{\mathrm{meas}} - V_{\mathrm{cell}} t_{\mathrm{exp}}, \tag{2}$$

where V_{cell} is the velocity parallel to flow, t_{exp} is the exposure time of the camera, and a_{meas} is the measured major axis length. Strictly speaking, the major axis might not align entirely with the velocity vector, in which case, the calculation would become more complicated. Even so, we believe this simple adjustment should mostly account for changes in eccentricity due to flow velocity. We performed eccentricity offset calibration based on velocity for CAR-T cell adhesion to E-selectin in Figs. 4 and 8.

In summary, MBM is a robust, easy-to-implement, high-throughput method to study cell adhesion dynamics in the presence of blood flow. Its flexibility allows for broad deployment in both

https://doi.org/10.1038/s41467-024-51014-4

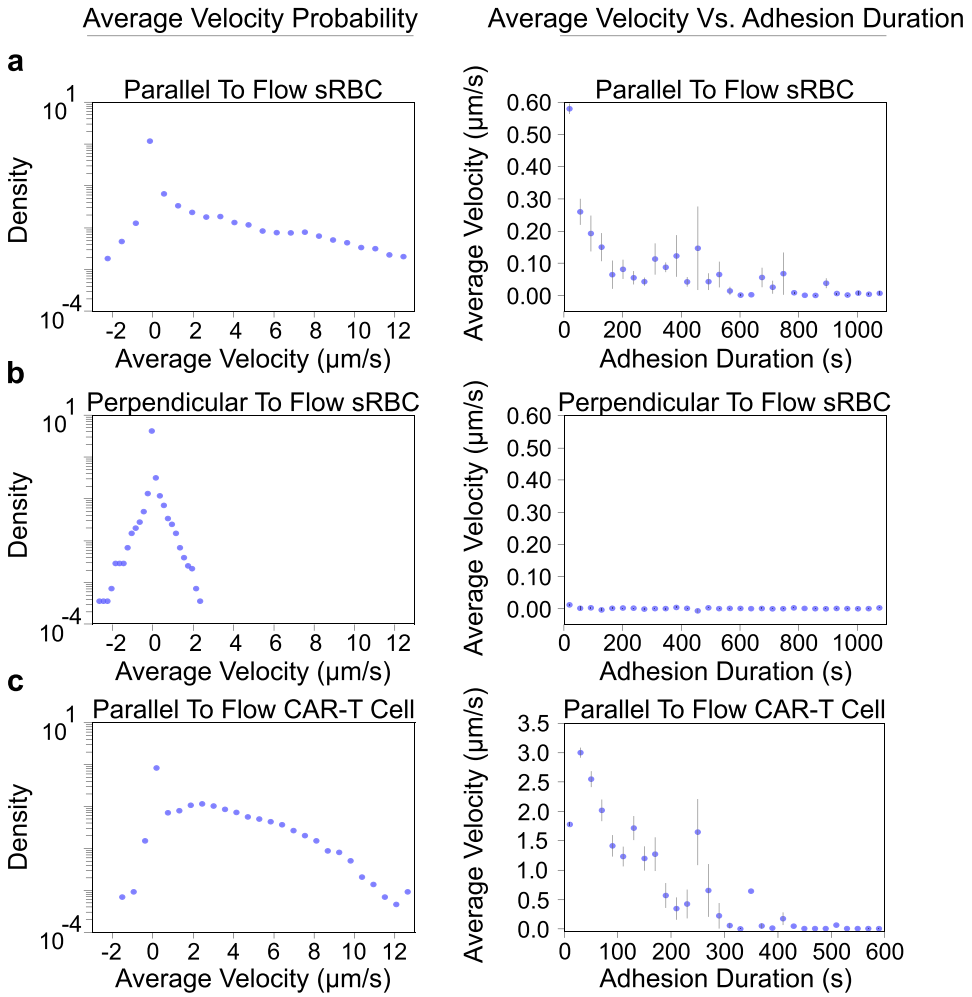

Fig. 9 | Velocities of cells under whole blood flow. Each row shows a velocity probability distribution (left) and a corresponding average velocity versus adhesion duration plot (right). Three cases are depicted: **a** Parallel to the flow direction for sickle red blood cell adhesion (sRBC) to laminin ($N = 14{,}229$). The probability distribution shows that a large majority of adhesion events have near-zero velocities. **b** Perpendicular to the flow direction for sickle red blood cell (sRBC) adhesion to laminin. Because this is the perpendicular to flow direction, we expect the distribution to approach that of a random walk, and the average velocities to be near zero. **c** Parallel to flow for CAR-T cell adhesion to E-selectin ($N = 7671$). When comparing this row to (**a**), we see that CAR-T cells adhering to E-selectin tend to have larger parallel to flow velocities. Perpendicular to flow analysis of CAR-T cells is not shown, but the results are similar to those of (**b**). Error bars denote one standard deviation.

clinical contexts and studies of fundamental biophysical mechanisms underlying cell adhesion. Combined with automated analysis for cell classification and tracking, it promises to be a general platform for elucidating how interactions with the complex whole blood environment influence and regulate cellular adhesion and interactions.

Methods

Blood sample collection and microfluidic adhesion assays

All research complies with the ethical regulations, approved by University Hospitals Institutional Review Board office (#05-14-07C). Surplus EDTA-anticoagulated whole blood samples were collected with the informed consent of the subjects under a protocol registered at www.clinicaltrials.gov as NCT02824471, "Sickle Cell Disease Biofluid Chip Technology". The microfluidic platforms were fabricated by lamination of 50 μm laser-cut double-sided adhesive film between APTES coated glass slide and 3.2 mm thick Poly(methyl methacrylate) (PMMA) cover[42]. Protein functionalization of the microchannels was achieved by injecting the channels with N-g-Maleimidobutyryloxy succinimide ester (0.28% vol/vol) followed by incubation with desired protein for 1.5 h at room temperature. For studying the adhesion of HbAA-containing red blood cells (healthy control with normal hemoglobin), unprocessed whole blood samples from healthy donors with no known hemoglobinopathies were used. For studying the adhesion of sRBCs, unprocessed whole blood samples from subjects with homozygous sickle cell disease (HbSS) were used and microchannels were coated with laminin (murine, laminin-1). For demonstrating Jurkat or CAR-T motility, the microchannels were coated with either P- or E-selectin (human, CD62P and CD62E). For microfluidic surface endothelialization, the channels were incubated overnight at 4 °C with 10% human fibronectin (Sigma-Aldrich). HUVECs (Lonza) were then seeded into each channel at a concentration of about 10 million cells/μL and channels were cultured under flow conditions created by a peristaltic pump for 2–3 days until confluent. Whole blood samples from subjects with no hemoglobinopathies were first leukodepleted and then premixed with Jurkat or CAR-T cell populations at 40% hematocrit in Hank's buffer containing calcium to retain the leukocyte activity by replenishing EDTA-depleted Ca++ in blood samples (Supplementary Fig. 7). HbSS whole blood was diluted 1:4 with PBS for the dilution experiment. Hypoxic conditions (SpO2 of ~83% in the blood sample), were achieved using an in-house developed micro-tube gas exchanger[23]. Highly gas permeable inlet tubing was fed through an impermeable tube which was connected to a 4 psi 95/5% N_2/CO_2

https://doi.org/10.1038/s41467-024-51014-4

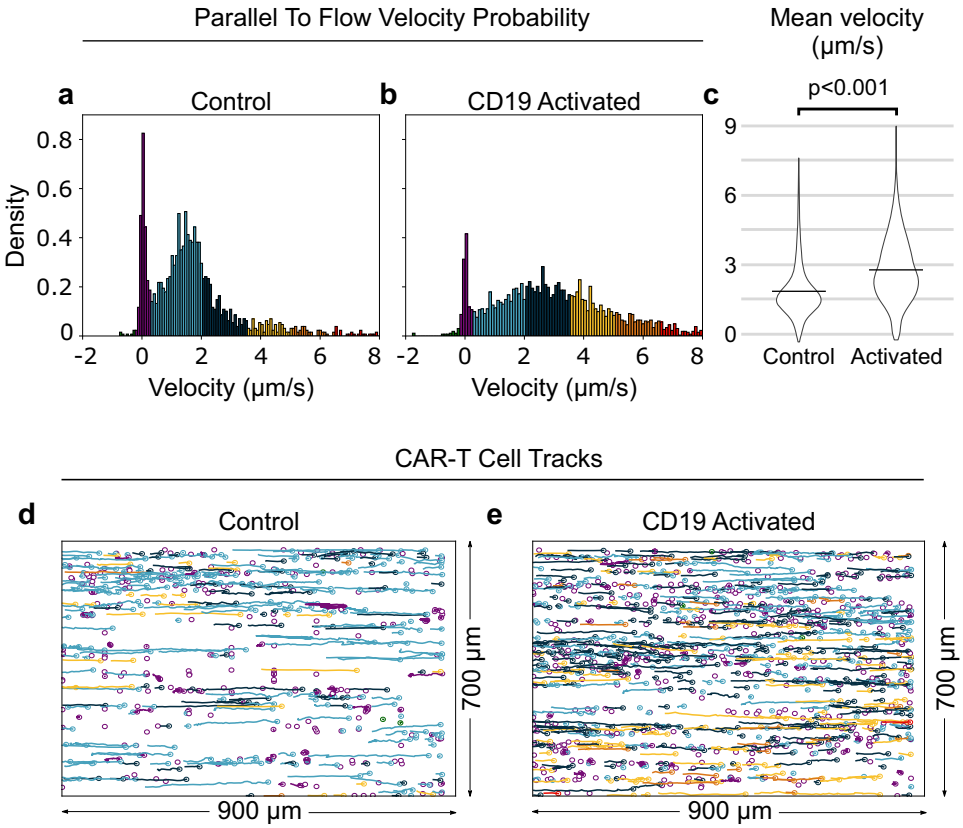

Fig. 10 | The effect of CD19 activation on the motility of CAR-T cells adhered to E-selectin. Velocity distribution of CAR-T cells for control (**a**) and CD19 activated (**b**) systems, with color coding highlighting different velocity ranges. **c** Activation leads to significantly increased mean rolling velocity among the rolling cells (1.85 ± 0.06 μm/s, $n = 1247$ vs. 2.77 ± 0.06 μm/s, $n = 2408$, data is mean ±95% CI, $p = 6 \times 10^{-85}$, black bars denote the means, *t*-test with two-tailed distribution without adjustments). Trajectories of adhered cells for the control (**d**) and activated (**e**) cases, labeled by their respective velocity ranges according to the same color scheme as in the distribution panels.

mixture source to allow parallel-flow gas exchange. To prevent non-specific cellular interactions, microchannels were incubated with bovine serum albumin at 4 °C overnight, and additionally, 250 μl of bovine serum albumin (20 mg/mL) was injected into the microchannels at room temperature with a 5 μl/min flow rate 2 h prior to the experiments.

CAR T-cell culture

CAR T-cells were obtained from the Hematopoietic Biorepository and Cellular Therapy core at Case Western Reserve University. These cells manufactured according to ethics and guidelines from University Hospitals Cleveland Medical Center (UHCMC IRB# 03-18-01C). Briefly, CD3+ T cells were collected from whole blood samples using the Miltenyi CD3 T cell isolation kit (North Rhine-Westphalia, Germany) and transduced with a CD19-directed CAR vector. Cells were cultured in TexMACS media with IL-7 and IL-15 (Miltenyi Biotec; North Rhine-Westphalia, Germany). Cells were then cryopreserved until experimentation. Upon thawing patient samples, cells were cultured in RPMI 1640 medium with 10% fetal bovine serum, 100 μ/mL pen/strep (Thermo Fisher, Waltham, MA, USA), 2 mM glutamax (Thermo Fisher, Waltham, MA, USA). For CD19 activation, CAR-T cells were added to a solution of IL-2 culture media containing CD19+ RAJI cells obtained from American Type Culture Collection (Manassas, VA, USA).

Motion blur microscopy

Microchannels were visualized with Olympus CellSens software using an Olympus IX83 inverted microscope and QImaging EXi Blue CCD camera with 10× objective (numerical aperture 0.3, pixel area 6.5 μm^2). To induce motion blur, camera exposure was set to 1.2 s. Images and videos of the microchannel surface were saved uncompressed to reduce noise. Frame rates of the videos were kept at (1/1.2) s^{-1}, which is the maximum frame rate for a 1.2 s exposure time. High integration time was compensated for by adjusting the voltage of the light source to 2.7 V (maximum 12 V). It should be noted that it is key to adjust the focus map for the surface of interest before the microchannels are injected with the sample. Unprocessed or leukodepleted whole blood was withdrawn into a syringe which then was loaded into a constant displacement syringe pump (NE-1000, New Era Pump Systems Inc.). MBM with automated analysis requires a minimum flow velocity of ~150 μm/s in the background to create the minimum particle streak for MBM. Higher background flow velocity yields better distinction of cellular interactions. 50/50 light distribution mode between the camera and the eyepieces was selected, which allows doubling the exposure time at the same brightness level. We performed all the experiments in a dark room. This is important because MBM is a low-light technique and room lights, or sunlight, may introduce non-uniformity to image lightness. The flow velocity was kept at ~500 μm/s for 20 min for demonstrating sRBC adhesion to laminin. For the demonstration of CAR-T cell adhesion to E-selectin, the flow velocity was swept linearly from 500 μm/s to 3500 μm/s in 10 min.

Automated image analysis

To analyze MBM images, we developed an automated analysis procedure with two distinct phases. Phase 1 performs segmentation on MBM images at the pixel level and phase 2 classifies groups of pixels by cell type. After classification, we can perform further analysis on the

classified cells (i.e., morphology characterization and trajectory tracking). While we focus on three experimental examples in this paper, our approach can easily be generalized to other systems.

Phase 1: pixel segmentation. Phase 1 uses a machine learning network to segment every pixel in an MBM image into one of two categories: adhered or background. Adhered pixels correspond to a pixel of the image belonging to an adhered object, with the remaining pixels falling into the background category.

The segmentation network is based on a modified U-Net architecture from our previous work[43] (further details are provided in the SI). To train the network, one or more MBM images are chosen as training/validation images, and the rest of the images are set aside for testing. A labeled mask of the training/validation images is created, by manually labeling each pixel as adhered or background. Each labeled training/validation mask, as well as each training/validation image, is then split into tiles of size 150 × 150 pixels, which are subsequently resized to 128 × 128 pixels, as that is the required input of the segmentation network. Once all of the training/validation tiles are compiled, we can then train the segmentation network for our particular task.

For the purposes of this paper, we have trained and used two distinct segmentation networks, one for analysis of sRBC adhesion to laminin, and one for analysis of CAR-T cell adhesion to E-selectin. The first network was trained/validated on tiles from a subset of 3 out of 177 MBM images. The training tiles are drawn from one of the three images, while the validation tiles are drawn from the two other images. The remaining 174 images were set aside for testing the network's ability to count adhered sRBCs (Fig. 5c). In total, there were 2163 tiles used for training/validation. The second network was trained on tiles from the frames of three MBM video sources. For each video source, ten evenly spaced frames were extracted from the final 100 frames, giving 30 frames in total for training/validation. The training tiles are drawn from one of the video sources, while the validation tiles are drawn from the two other video sources. 169 of the remaining frames from one of the video sources were set aside for testing the network's ability to count adhered CAR-T cells (Fig. 5d). In total, there were 767 tiles used for training/validation. In both cases we implemented a stratified split of 70%/20%/10% training/validation1/validation2, where validation set 1 was used for validating during individual training sessions, and validation set 2 was used for comparing trained models against one another for the purposes of hyperparameter optimization.

Phase 2: cell classification. The output of the segmentation network is a fully segmented image, where each pixel belongs to one of two classes. In the second phase of the analysis, groups of adhered pixels are extracted and classified. Generally speaking, the cell identification task falls into one of two cases. In the first case, only one adhered cell type is expected to be distinguishable in the MBM image. In the second case, two or more cell types are expected to be distinguishable in the MBM image. For brevity, we will only highlight the single-cell type case in the main text, and interested readers can refer to the SI for information on the multiple-cell type case.

When only a single cell type of interest is expected to adhere to the functionalized channel, we can classify groups of adhered pixels using a physical property of the group. For example, when we look at the attachment of sRBCs to laminin or CAR-T cells to E-selectin, the vast majority of groups of adhered pixels correspond to one cell type. In this case, we can use a size threshold to distinguish adhered cells from groups of adhered pixels falsely classified by the segmentation network as adhered.

When training both segmentation networks, the size threshold for the classification of groups of adhered pixels was optimized with the objective to produce the closest agreement between human and machine counts of relevant cells. To find the optimum threshold, an array of threshold values can be used to count cells for an array of inputs. The automated cell counts can then be compared to manual cell counts, and the threshold which produces the greatest agreement can be chosen. For single-cell type analysis, two optimum thresholds were found, one for sRBC adhesion to laminin and one for CAR-T cell adhesion to E-selectin.

In the laminin case, 174 MBM images were analyzed using a trained segmentation network, and size thresholds in the range 0–200 px (corresponding to the area of the adhered pixel group), in increments of ten, were used to produce sRBC counts. Agreement between human and machine counts was checked for each threshold value, and the optimum threshold was found to be 90 pixels (38 μm^2), where groups of adhered pixels with a size greater than 90 pixels were classified as sRBCs, and groups of adhered pixels with size less than 90 pixels were classified as other. For the CAR-T case, 172 frames from an MBM video were analyzed using a trained segmentation network, and size thresholds in the range 0–200 px, in increments of ten, were used to produce CAR-T cell counts. The optimum threshold was found to be 30 pixels (13 μm^2).

Post-classification analysis. After phase 1 and phase 2 are completed, the groups of adhered pixels that are positively classified as the cell type(s) of interest can be further analyzed. Properties like the size, eccentricity, and position of each individual cell are easily obtainable. These static data can be analyzed individually or aggregated together to produce group statistics. When MBM video is available, we can analyze the dynamics of cells under flow. We define a parameter for each adhesion event called the survival time −the time from when a cell attaches to the surface until it detaches or leaves the frame. With the survival time in hand, as well as the static data for each frame, we can generate dynamic data for each cell. Individual cell dynamics like average velocity, average size, and average eccentricity can be found, or, we can aggregate cells and produce group statistics like mean-squared displacement, or distributions of dynamic quantities.

Identification rules for tracking moving cells in MBM videos. MBM video analysis brings forth additional challenges beyond those of individual images. In particular, we need to track cells over time, requiring us to determine if cells in consecutive frames are the same cell or not. Two distinct issues arose when making this determination: duplicate counts, and tracking motile cells.

Duplicate counts occur when the segmentation network erroneously segments a single group of adhered pixels as two distinct groups of adhered pixels, whose edges are close, but not touching. To minimize the duplicate counts, we checked to see if the centroids of any two groups of adhered pixels were within 50 pixels (1 px = 0.322 μm) of one another. Also, the shortest distance between the edges of all such pairs was computed, and if this distance was 5 pixels or fewer for any pair, the two groups of adhered pixels were considered to be one. In this case, the two groups of adhered pixels were replaced by the smallest polygon that contains them, known as the convex hull. One can imagine this shape as the result of stretching a rubber band over the two groups of adhered pixels and letting it rest taut.

Another case of duplicate counting occurs if phase 2 misclassified an adhered cell as other for any amount of frames between two positive classifications. This error would cause the analysis to detect a new group of adhered pixels, despite it being the same cell. We avoid this by giving each adhesion event a disappearance allowance. Each cell for an adhesion event was allowed to disappear for a number of frames before considering the adhesion event completed. If a cell disappeared for a number of frames below the allowance and then reappeared, the adhesion event would continue as if the misclassification never occurred. For sRBCs, we allowed cells to go undetected for up to two frames and still count as the same cell. For CAR-T cells, they could go

undetected for up to nine frames. These frame thresholds helped us to not preemptively end adhesion events.

Interacting motile cells are constantly adhering, detaching, and persisting in their adhesion to the surface, and as such, the results of analyzing many frames present a complex picture of many adhesion events happening at various times. Thus, we devised rules by which to determine if a cell in consecutive frames was a new adhesion event or a continuation of a prior adhesion event. If a positively identified group of adhered pixels was within 5 pixels in any direction of a positively identified group of adhered pixels in the previous frame, the group of adhered pixels was classified as a continuation of the adhesion event. Otherwise, the positively identified group of adhered pixels was classified as the beginning of a new adhesion event. Also, if a positively identified group of adhered pixels was within 5 to 30 pixels in the direction of the flow, this group of adhered pixels was classified as a motile adhesion event. These movement rules plus the frame thresholds protected us from splitting a singular adhesion event into two due to any misclassifications by the automated analysis.

Statistical methods

Statistical analyses were performed using the Microsoft Excel Real Statistics Resource Pack add-in. $p < 0.05$ was chosen to indicate a significant difference.

Reporting summary

Further information on research design is available in the Nature Portfolio Reporting Summary linked to this article.

Data availability

Raw image data and all data generated in this study are available at the Open Science Framework repository: https://osf.io/uy3rx. Source data are provided with this paper.

Code availability

All the code associated with the MBM analysis can be found at: https://github.com/hincz-lab/motion-blur-microscopy[44].

References

1. Sai, J., Rogers, M., Hockemeyer, K., Wikswo, J. P. & Richmond, A. Study of chemotaxis and cell–cell interactions in cancer with microfluidic devices. in *Methods in Enzymology*, vol. 570 (Elsevier, 2016).
2. Hines, P. C. et al. Flow adhesion of whole blood to P-selectin: a prognostic biomarker for vaso-occlusive crisis in sickle cell disease. *Br. J. Haematol.* **194**, 1074–1082 (2021).
3. Man, Y. et al. Leukocyte adhesion to P-selectin and the inhibitory role of crizanlizumab in sickle cell disease: A standardized microfluidic assessment. *Blood Cells Mol. Dis.* **83**, 102424 (2020).
4. Hernandez, A. A. et al. An allosteric shift in CD11c affinity activates a proatherogenic state in arrested intermediate monocytes. *J. Immunol.* **205**, 2806–2820 (2020).
5. Barshtein, G., Zelig, O., Gural, A., Arbell, D. & Yedgar, S. Determination of red blood cell adhesion to vascular endothelial cells: A critical role for blood plasma. *Colloids Surf. B Biointerfaces* **210**, 112226 (2022).
6. Gutierrez, M., Fish, M. B., Golinski, A. W. & Eniola-Adefeso, O. Presence of rigid red blood cells in blood flow interferes with the vascular wall adhesion of leukocytes. *Langmuir* **34**, 2363–2372 (2018).
7. Buscher, K., Marcovecchio, P., Hedrick, C. C. & Ley, K. Patrolling mechanics of non-classical monocytes in vascular inflammation. *Front. Cardiovasc. Med.* **4**, 80 (2017).
8. Cabrales, P. et al. The macrophage stimulating anti-cancer agent, RRx-001, protects against ischemia-reperfusion injury. *Expert Rev. Hematol.* **10**, 575–582 (2017).
9. Cheburkanov, V., Keene, E., Pipal, J. & Yakovlev, V. V. Towards in vivo larynx imaging: assessing mechanical properties of larynx with Brillouin microscopy. in *Optical Biopsy XX: Toward Real-Time Spectroscopic Imaging and Diagnosis*, vol. 11954 (SPIE, 2022).
10. Hwang, K. et al. Handheld endomicroscope using a fiber-optic harmonograph enables real-time and in vivo confocal imaging of living cell morphology and capillary perfusion. *Microsyst. Nanoeng.* **6**, 1–11 (2020).
11. Wang, F. et al. In vivo NIR-II structured-illumination light-sheet microscopy. *Proc. Natl Acad. Sci.* **118**, e2023888118 (2021).
12. Condeelis, J. & Weissleder, R. In vivo imaging in cancer. *Cold Spring Harb. Perspect. Biol.* **2**, a003848 (2010).
13. Sundd, P. et al. 'Slings' enable neutrophil rolling at high shear. *Nature* **488**, 399–403 (2012).
14. da Silva, B. C. G., Tam, R. & Ferrari, R. J. Detecting cells in intravital video microscopy using a deep convolutional neural network. *Comput. Biol. Med.* **129**, 104133 (2021).
15. Gregorio da Silva, B. C., Carvalho-Tavares, J. & Ferrari, R. J. Detecting and tracking leukocytes in intravital video microscopy using a Hessian-based spatiotemporal approach. *Multidimens. Syst. Signal Process.* **30**, 815–839 (2019).
16. Jennissen, H., Sanders, A., Schnittler, H. & Hlady, V. TIRF-rheometer for measuring protein adsorption under high shear rates: constructional and fluid dynamic aspects. *Mater. Werkst. Entwickl. Fert. Pr.üfung Eigenschaften Anwend. Tech. Werkst.* **30**, 850–861 (1999).
17. Pisapati, A. V. et al. Characterizing single-molecule conformational changes under shear flow with fluorescence microscopy. *J. Vis. Exp.* **155**, e60784 (2020).
18. Avtaeva, Y. N., Mel'nikov, I., Okhota, S., Zozulya, N. & Gabbasov, Z. Kinetics of platelet adhesion to protein-coated surface in whole blood samples at high flow rates. *Bull. Exp. Biol. Med.* **169**, 229–232 (2020).
19. Goreke, U., Bode, A., Yaman, S., Gurkan, U. A. & Durmus, N. G. Size and density measurements of single sickle red blood cells using microfluidic magnetic levitation. *Lab Chip* **22**, 683–696 (2022).
20. Man, Y. et al. Occlusionchip: a functional microcapillary occlusion assay complementary to ektacytometry for detection of small-fraction red blood cells with abnormal deformability. *Front. Physiol.* **13**, 954106 (2022).
21. An, R. et al. Sickle red blood cell-derived extracellular vesicles activate endothelial cells and enhance sickle red cell adhesion mediated by von Willebrand factor. *Br. J. Haematol.* **201**, 552–563 (2023).
22. Center for Drug Evaluation and Research (CDER), Center for Veterinary Medicine (CMV). *Guidance for Industry, Bioanalytical Method Validation* (U.S. Department of Health and Human Services, Food and Drug Administration, 2018).
23. Goreke, U. et al. Membrane bending and sphingomyelinase-associated, sulfatide-dependent hypoxic adhesion of sickle mature erythrocytes. *Blood Adv.* **7**, 2094–2104 (2023).
24. Sharpe, A. H. & Pauken, K. E. The diverse functions of the PD1 inhibitory pathway. *Nat. Rev. Immunol.* **18**, 153–167 (2018).
25. You, R. et al. Active surveillance characterizes human intratumoral T cell exhaustion. *J. Clin. Investig.* **131**, e144353 (2021).
26. Wong, K. H., Chan, J. M., Kamm, R. D. & Tien, J. Microfluidic models of vascular functions. *Annu. Rev. Biomed. Eng.* **14**, 205–230 (2012).
27. Goreke, U. et al. Catch bonds in sickle cell disease: shear-enhanced adhesion of red blood cells to laminin. *Biophys. J.* **122**, 2564–2576 (2023).
28. Bekassy, Z., Lopatko Fagerström, I., Bader, M. & Karpman, D. Crosstalk between the renin–angiotensin, complement and kallikrein–kinin systems in inflammation. *Nat. Rev. Immunol.* **22**, 411–428 (2022).
29. Bell, G. Models for the specific adhesion of cells to cells. *Science* **200**, 618–27 (1978).

30. Hillringhaus, S., Dasanna, A. K., Gompper, G. & Fedosov, D. A. Stochastic bond dynamics facilitates alignment of malaria parasite at erythrocyte membrane upon invasion. *eLife* **9**, e56500 (2020).
31. Anvari, S., Osei, E. & Maftoon, N. Interactions of platelets with circulating tumor cells contribute to cancer metastasis. *Sci. Rep.* **11**, 1–16 (2021).
32. Lansche, C. et al. The sickle cell trait affects contact dynamics and endothelial cell activation in Plasmodium falciparum-infected erythrocytes. *Commun. Biol.* **1**, 1–14 (2018).
33. Strnad, M. et al. Nanomechanical mechanisms of Lyme disease spirochete motility enhancement in extracellular matrix. *Commun. Biol.* **4**, 1–9 (2021).
34. Arora, N., Hazra, J. P. & Rakshit, S. Anisotropy in mechanical unfolding of protein upon partner-assisted pulling and handle-assisted pulling. *Commun. Biol.* **4**, 1–10 (2021).
35. Yang, J. et al. Molecular interaction and inhibition of SARS-CoV-2 binding to the ACE2 receptor. *Nat. Commun.* **11**, 1–10 (2020).
36. Li, N. et al. Ligand-specific binding forces of LFA-1 and Mac-1 in neutrophil adhesion and crawling. *Mol. Biol. Cell* **29**, 408–418 (2018).
37. Priyadarshani, J., Roy, T., Das, S. & Chakraborty, S. Frugal approach toward developing a biomimetic, microfluidic network-on-a-chip for in vitro analysis of microvascular physiology. *ACS Biomater. Sci. Eng.* **7**, 1263–1277 (2021).
38. Paggi, C. A., Teixeira, L. M., Le Gac, S. & Karperien, M. Joint-on-chip platforms: entering a new era of in vitro models for arthritis. *Nat. Rev. Rheumatol.* **18**, 217–231 (2022).
39. Vu, H. T., Chakrabarti, S., Hinczewski, M. & Thirumalai, D. Discrete step sizes of molecular motors lead to bimodal non-gaussian velocity distributions under force. *Phys. Rev. Lett.* **117**, 078101 (2016).
40. Kok, R. et al. OrganoidTracker: efficient cell tracking using machine learning and manual error correction. *PLoS ONE* **15**, e0240802 (2020).
41. Aragaki, H., Ogoh, K., Kondo, Y. & Aoki, K. LIM tracker: a software package for cell tracking and analysis with advanced interactivity. *Sci. Rep.* **12**, 2702 (2022).
42. Alapan, Y. et al. Sickle cell disease biochip: a functional red blood cell adhesion assay for monitoring sickle cell disease. *Transl. Res.* **173**, 74–91 (2016).
43. Praljak, N. et al. Integrating deep learning with microfluidics for biophysical classification of sickle red blood cells adhered to laminin. *PLoS Comput. Biol.* **17**, e1008946 (2021).
44. Shipley, B. & Gonzales, A. Motion blur microscopy, motion-blur-microscopy, https://doi.org/10.5281/zenodo.11642913 (2024).

Acknowledgements

We express deep gratitude to Paolo F. Caimi at the Case Comprehensive Cancer Center and Cleveland Clinic, Jane Reese Koc at the Hematopoietic Biorepository and Cellular Therapy Core at Case Western Reserve University for sharing the CAR-T cells, and to Paul Tesar at the Case Western Reserve University School of Medicine for sharing the cell culture resources. This work was supported by the National Institutes of Health awards U01AI176469, R42HL162214, R42HL160384, K25HL159358, and National Science Foundation awards 1552782, 1651560, 2112202, 2332121. The authors acknowledge with gratitude the contributions of research participants and clinicians at Seidman Cancer Center (University Hospitals Cleveland Medical Center).

Author contributions

U.G. and U.A.G. developed the idea. U.G., B.S., A.G., M.H., and U.A.G. designed the study. U.G., M.T., O.S., W.J.W., and Y.M. performed the experiments. U.G., B.S., A.G., and M.H. developed the automated algorithm. U.G., B.S., A.G., M.T., O.S., Y.M., W.J.W., R.A., M.H., and U.A.G. analyzed the data. U.G., B.S., A.G., M.T., O.S., W.J.W., M.H., and U.A.G. discussed and interpreted the data. U.G., B.S., A.G., wrote the manuscript, U.G., B.S., A.G., prepared the figures. M.H. and U.A.G. edited the manuscript.

Competing interests

R.A., U.A.G., and Case Western Reserve University have financial interests in Hemex Health Inc. U.A.G., and Case Western Reserve University have financial interests in BioChip Labs Inc. U.A.G. and Case Western Reserve University have financial interests in Xatek Inc. U.A.G. has financial interests in DxNow Inc. Financial interests include licensed intellectual property, stock ownership, research funding, employment, and consulting. Hemex Health Inc. offers point-of-care diagnostics for hemoglobin disorders, anemia, and malaria. BioChip Labs Inc. offers commercial clinical microfluidic biomarker assays for inherited or acquired blood disorders. Xatek Inc. offers point-of-care global assays to evaluate the hemostatic process. DxNow Inc. offers microfluidic and bioimaging technologies for in vitro fertilization, forensics, and diagnostics. The competing interests of Case Western Reserve University employees are overseen and managed by the Conflict of Interests Committee according to a Conflict-of-Interest Management Plan. The remaining authors declare no competing interests.

Additional information

Supplementary information The online version contains supplementary material available at https://doi.org/10.1038/s41467-024-51014-4.

Correspondence and requests for materials should be addressed to Michael Hinczewski or Umut A. Gurkan.

Peer review information *Nature Communications* thanks Nikita Genze, and the other, anonymous, reviewer(s) for their contribution to the peer review of this work. A peer review file is available.